Nanostructured Zr-Cu metallic glass thin films with tailored electrical and optical properties

Alejandro Borroto, S. Bruyère, S. Migot, C. de Melo, David Horwat, J.F. Pierson

Nanostructured Zr-Cu metallic glass thin films with tailored electrical and optical properties

A. Borroto [a, b], S. Bruyère [a], S. Migot [a], C. de Melo [a, c], D. Horwat [a], and J.F. Pierson [a,*]

[a] Université de Lorraine, CNRS, IJL, F-54000 Nancy, France.

[b] Univ Rennes, CNRS, IETR-UMR 6164, F-35000 Rennes, France.

[c] Interfaces, Confinement, Matériaux et Nanostructures, ICMN, UMR 7374, Université d'Orléans, CNRS, 1b rue de la Férollerie, F-45071 Orléans, France.

*jean-francois.pierson@univ-lorraine.fr

Abstract

Nanostructured metallic glass thin films (NMGTF) have attracted increasing attention because they are amorphous materials of tunable microstructure, which allows tailoring their properties. Herein, we provide new insights into the formation of Zr-Cu NMGTF deposited by magnetron sputtering. By varying over a wide range the working-gas pressure during the sputtering process (from 0.3 to 2 Pa) and the alloy composition (from ~16 to 94 at.% Cu), we show that the film microstructure can be tuned from homogeneous and compact to nanostructured, formed by nanocolumns. In particular, we demonstrate that the formation of nanocolumnar glassy films is promoted at high working pressures and low Cu contents. In addition, transmission electron microscopy and X-ray diffraction analyses reveal that the microstructural transition from homogeneous to nanocolumnar films leads to an increase in the full-width at half-maximum of the first diffraction peak, suggesting a change in the local order of the glassy alloys. Furthermore, we prove that the microstructural change allows the electrical resistivity and the optical reflectance of the films to be tailored to a large extent. We show that the amorphous films exhibit a linear relationship between their reflectance and the

square root of the resistivity, according to the free electron model. However, this linear relationship breaks down for high resistivity values, for which the reflectance no longer depends on the resistivity. We highlight that, by changing the working pressure, the electrical resistivity and optical reflectance can be tuned following the same scaling law, whatever the composition of the alloy. Our results shed light on the microstructure-properties relationship of NMGTF and could serve as a platform for future applications in the field of optoelectronics.

Keywords: Zr-Cu alloys, Nanostructured metallic glass thin films, Electrical properties, Optical properties, Microstructural control.

1. Introduction

It is a truth universally acknowledged that microstructure defines properties of materials. This paradigm has been largely used in crystalline materials, for which microstructural control through defect incorporation (such as dislocations or grain boundaries) has served as a roadmap to tailor their properties [1–5]. An extreme case is nanocrystalline materials, in which the proportion of atoms located at the grain boundaries or affected by it is comparable to the atoms forming the core of crystallites, a condition obtained by reducing the size of the crystallites of a polycrystalline material to a few nanometers [6]. Nanocrystalline materials have been proven to have enhanced and/or novel properties compared to their single-crystal or polycrystalline counterparts, triggered by the different atomic arrangement caused by the incorporation of grain boundaries [7–10]. Inspired by the idea of nanocrystalline materials, Gleiter and coworkers have developed the concept of nanoglasses (NG): a new class of metallic glasses consisting in nanometer-sized glassy regions connected by glass/glass interfaces of higher free volume, i.e. lower density [11–19]. The NG concept challenges that of traditional metallic glasses, which are known to present structural heterogeneity at the atomic scale (at the short and medium-range order) but nevertheless exhibit a uniform and homogeneous microstructure. Controlling the microstructure and consequently the properties by tailoring the glass/glass interfaces adds a new feature to traditional metallic glasses, which has opened a new avenue in the field of amorphous alloys [20–25].

NG have been produced traditionally by inert gas condensation (IGC), which involves two main steps: first, condensation on a cold finger of nano-sized glassy clusters generated by evaporation (or sputtering) in an inert gas atmosphere and, second, consolidation (after scraping off from the cold finger) of the glassy nano-clusters in a high-pressure device [12]. Besides the IGC method for obtaining NG, other synthesis routes have been used that allow

nanostructuring metallic glasses through the incorporation of glass/glass interfaces, but which may present some differences with respect to traditional NG. For example, cluster-assembled metallic glasses (CAMG) [26–29] synthesized by energetic impact of clusters on a substrate, instead of mechanical consolidation as in IGC, are composed of glassy nano-clusters of smaller size compared to those of NG. Magnetron sputtering has been also used to synthesize nanostructured metallic glass thin films (NMGTF) [30–41]. In contrast to traditional NG, which present a microstructure comprised of spheroidal nanoclusters, sputter-deposited NMGTF exhibit a nanocolumnar microstructure [35–41].

The role of glass/glass interfaces in the properties of sputter-deposited NMGTF has been highlighted by several authors. For example, Wang *et al.* showed that Au-based NMGTF exhibit enhanced thermal stability compared to its melt-spun ribbon counterpart [33]. Ketov *et al.* demonstrated that Zr-Pd NMGTF present good catalytic activity and biocompatibility [34]. Rauf *et al.* reported good mechanical performance and excellent soft magnetic properties in Fe-Zr NMGTF [39]. In addition to the intrinsic control of properties due to the presence of glass/glass interfaces, it has been recently demonstrated that such interfaces can influence the surface topography evolution of $Zr_{65}Cu_{35}$ films under ultrafast laser irradiation [42,43]. In particular, Prudent *et al.* have proved that regularly distributed nanowells spontaneously form on the surface of the film, which could have promising applications for the storage and detection of chemical or biological elements [43].

A distinctive feature of sputter-deposited NMGTF is that, with precise control of the deposition parameters during the sputtering process, the film microstructure can be tuned to become homogeneous and featureless [36–38,40,41]. This has been proven, for example, in glassy Ni-Nb [41] and Au-based [38] thin films through substrate temperature or working-gas pressure control. However, in all these studies the microstructural transition from homogeneous to nanostructured amorphous films was investigated in alloys with specific

compositions. The role of alloy composition on the microstructural evolution and associated properties has not been explored so far. We accomplished this in our work. By using binary Zr-Cu alloys, a well-known glass former system [44] for which NG formation by IGC has already been reported [45–47], we investigated over a wide range of alloy compositions (from ~16 to 94 at.% Cu) the impact of the microstructural transition on the evolution of the structure, electrical and optical properties of the films. Our results revealed a change in the local order of the glassy alloys and highlighted the possibility provided by the microstructural transition from homogeneous to nanostructured to tailor the electrical resistivity and optical reflectance of nanostructured metallic glass thin films.

2. Experimental details

2.1. Thin film synthesis

Binary Zr-Cu alloys were obtained by DC magnetron co-sputtering of Zr and Cu metallic targets in an argon atmosphere. The films were deposited on (100)-oriented silicon single crystal substrates of 1.5×1.5 cm^2. Although the two cathodes were in confocal configuration, the depositions were done with the substrate holder in rotating mode to guarantee homogeneity of the films. The sputtering chamber was pumped down via a mechanical and a turbo-molecular pumps allowing a base vacuum of 10^{-6} Pa. A target-to-substrate distance of 9 cm was fixed for all the experiments. To achieve microstructural control of the films, the working argon pressure was varied between 0.3 and 2 Pa. The alloy composition was controlled by varying the discharge current applied to the Cu target between 0.02 and 0.7 A, while that of the Zr target was kept constant at 0.3 A (target dimensions: 50.8 mm in diameter, 3 mm-thick and purity higher than 99.9%, both were powered by a Maxim 1000 DC generator). The deposition time was calibrated to obtain films of ~1 μm thickness. The films were deposited without external heating and without substrate bias during deposition. The self-established temperature at the substrate was measured using a thermocouple and did not exceed 45 °C during growth. Details on the film synthesis parameters, as well as film thicknesses and compositions are listed in Table SI, Supplementary Information.

2.2. Thin film characterization

X-ray diffraction measurements were conducted in the Bragg-Brentano configuration with K_αCu radiation (λ=1.5406 Å) using an AXS Bruker D8 Advance diffractometer. To analyze the collected data, the diffraction angle 2θ was converted to momentum vector, q, via $q = 4\pi\times\sin\theta/\lambda$, where λ is the X-ray wavelength. The position of the first diffraction peak and its corresponding full-width at half-maximum were determined by fitting a Gaussian-Lorentzian sum function, after background subtraction [48]. Top and cross-section views of the films

were obtained by scanning electron microscopy (SEM) using a ZEISS Gemini SEM 500 equipped with field emission gun at an accelerating voltage of 2.0 kV. The chemical composition of the films was determined using an energy dispersive X-ray spectroscopy (EDS) coupled to the scanning electron microscope. The EDS measurement was carried out at an accelerating voltage of 20 kV. The thickness of the films was measured using a Bruker DektakXT tactile profilometer and confirmed with cross-section SEM observations. Thickness and composition were measured in at least three different positions along the films. Transmission electron microscopy (TEM) analysis was performed using a JEOL-ARM 200 Cold FEG TEM/STEM operating at 200 kV and equipped with two spherical aberration (Cs) probe correctors (point resolution 0.12 nm in TEM mode and 0.078 nm in STEM mode). For this analysis, cross-section TEM samples of films were prepared using a focused ion beam (FIB)-scanning electron microscope dual beam system (FEI Helios NanoLab 600i).

The density of selected samples was determined by X-ray reflectivity (XRR). XRR measurements were performed in a PANanalytical X'Pert Pro MRD diffractometer using $K_{\alpha}Cu$ radiation (λ=1.5406 Å). This diffractometer is equipped with a 4-circles goniometer which allows a precise orientation of the samples and the measurements were performed in symmetrical (θ-2θ) configuration for angles close to the critical angle of total reflection. The fits to the experimental XRR curves (Fig. S1, Supplementary Information) were made with the PanAnalytical software X'Pert Reflectivity (using the film thickness, density and roughness as fitting parameters). Residual stress measurements were performed in films deposited on Si substrates (100-oriented) of 200 μm thickness and 0.5×2.5 cm^2. Thus, residual stress was calculated using Stoney's equation [49], $\sigma = M_s/6\times h_s^2/h_f \times(1/R\text{-}1/R_0)$, where h_f is the film thickness, h_s is the substrate thickness, M_s = 180.3 GPa is the biaxial modulus of the substrate, R_0 is the curvature radius of the substrate before film deposition, and R is the

curvature radius after film deposition. Film thicknesses and curvature radii were measured using a DektakXT BRUKER profilometer.

The total reflectance (specular reflectance + diffuse reflectance) of the films was measured in the 350-2500 nm wavelength range using a Varian Cary 7000 UV-vis-NIR spectrophotometer with an integrating sphere coupled. The electrical resistivity, ρ, was calculated from the sheet resistance, R_s, using equation: $\rho = R_s \times t$, where t is the film thickness [50]. R_s was determined using the four-point probe method in a linear contact configuration as: $R_s = C \times V/I$, where I is the current applied through the outer contacts, V the resulting voltage measured at the inner contacts, and C is a correction factor due to the contact geometry and the geometry of the sample. In our case (substrate dimension: 1.5×1.5 cm^2 and points spacing of 1 mm) C = 4.3882 [50].

3. Results and discussion

3.1. Formation of nanostructured Zr-Cu metallic glass thin films

The microstructure of sputter-deposited films is determined by the deposition parameters of the sputtering process. In particular, the working-gas pressure plays a major role in the microstructural control of the films obtained. An increase in the working pressure results in a decrease in the mean free path of the sputtered atoms. Therefore, the number of collisions they experience with the working-gas atmosphere (argon in our case) increases, thereby decreasing their kinetic energy upon reaching the substrate (Fig. 1a). Consequently, the surface diffusivity of adatoms on the substrate decreases, which has an impact on the microstructure of the growing film. Fig. 1b shows cross-sectional transmission electron microscopy (TEM) images and corresponding selected-area electron diffraction (SAED) patterns of Zr-Cu films with the same composition (50 at.% Cu) but deposited at different working pressures (0.3, 1.0, and 2.0 Pa). The micrographs show that the microstructure of the films changed from compact and homogeneous to a more voided one, formed by nanocolumns, when the working pressure was increased (Fig. 1b, left panel). Regardless of the microstructural change, all the films were amorphous, as evidenced by the diffuse ring of the SAED patterns (Fig. 1b, right panel).

To explore a possible variation in the local structural order of the amorphous films, we extracted the intensity profiles of the regions highlighted in the SAED patterns (Fig. 1c). From the profiles, we determined the full-width at half-maximum, Δq, of the first diffraction peak. Δq has been suggested to be a measure of the dispersion of the structural units forming the amorphous structure, being an indicator of the glass forming ability (GFA) [48]. According to Fig. 1d, Δq increased with increasing working pressure. This result indicated that, in addition to the microstructural variation, the local order changes as well, evidenced by a greater dispersity of the structural units comprising the amorphous phase. The tendency for

Δq to increase with increasing pressure was also corroborated using X-ray diffraction analysis, and a more thorough discussion regarding this will be done later in this paper.

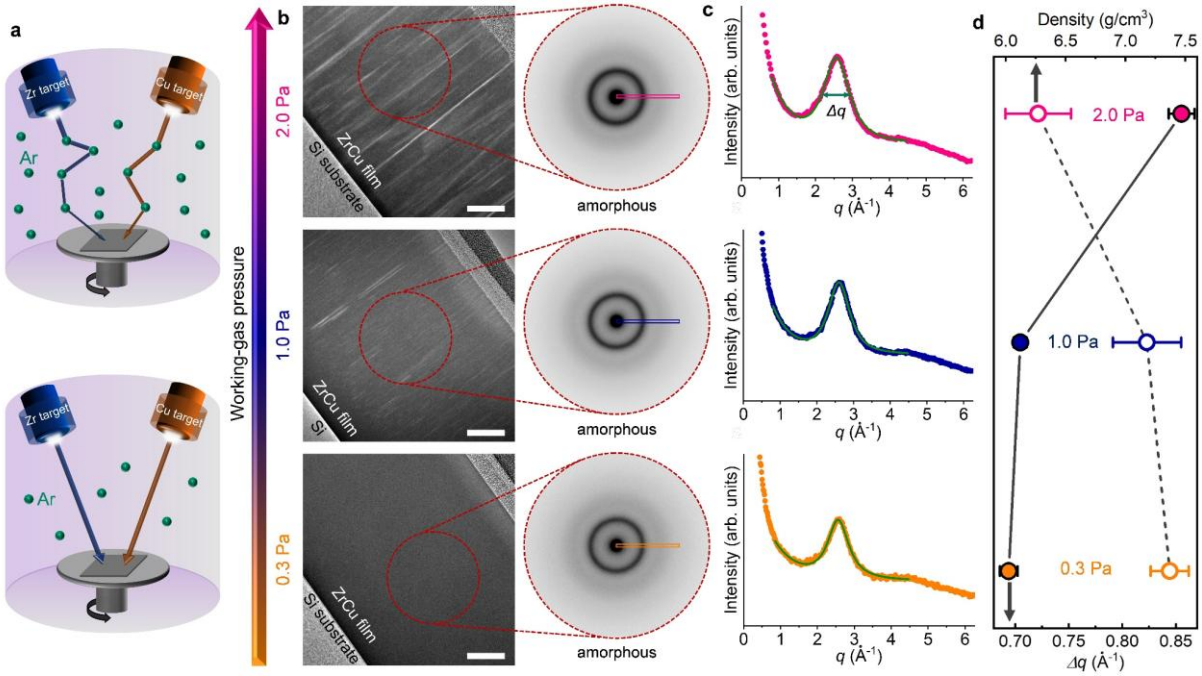

Figure 1. Microstructural control in Zr-Cu thin film metallic glasses. (a) By increasing the working-gas pressure of the magnetron sputtering process, the mean free path of the sputtered atoms decreases. As a result, their kinetic energy when arriving at the substrate also decreases, which allows the microstructure of the films to be tuned. (b) Cross-sectional TEM images (left) and corresponding SAED patterns (right) of $Zr_{50}Cu_{50}$ films deposited at 0.3, 1.0, and 2.0 Pa. The TEM images reveal that the microstructure of the films changes from homogeneous to nanostructured, formed by nanocolumns, with increasing working pressure. Scale bar: 200 nm. The diffuse ring in the SAED patterns evidences the amorphous nature of the films. (c) Intensity profiles extracted from the regions highlighted in the SAED patterns. Higher intensity in the profiles means darker contrast in the SAED patterns. The green curves represent the fittings to the diffraction peaks from which the full-width at half-maximum, Δq, can be extracted. (d) Evolution with working-gas pressure of the density of the films and Δq.

The microstructural change that occurs with increasing working pressure was also evidenced by a decrease in film density (Fig. 1d). The density of the film deposited at 0.3 Pa was 7.37±0.16 g/cm^3 which is in the order of the values reported for ribbons (7.33 g/cm^3) [51] and thin films (7.23 g/cm^3) [44] of Zr-Cu alloys with the same composition. However, the film deposited at 2.0 Pa presented a density of 6.30±0.40 g/cm^3. This decrease can be attributed to

the appearance, with increasing working pressure, of the interfaces (of lower density) between the nanocolumns formed.

The transition from homogeneous to nanocolumnar amorphous films, presented so far in alloys with 50 at.% Cu, also occurs in films with different compositions. Fig. 2 shows top and cross-section view SEM images of Zr-Cu thin films with 35, 50, 65, and 80 at.% Cu deposited at different working pressures. Overall, the change in microstructure with working pressure was observed in all the compositions studied. In addition, some films showed a compact microstructure from the cross-section images, but a granular morphology from the surface view (see, for example, 35 at.% Cu film obtained at 0.5 Pa, 65 at.% Cu film obtained at 1.0 Pa, or 80 at.% Cu film obtained at 2.0 Pa). We can notice that these films were obtained at working pressures between those that allow obtaining compact films with smooth surfaces and those that allow obtaining nanocolumnar films.

Microstructural control of sputter-deposited polycrystalline films with the working-gas pressure (or any other parameter that causes a change of kinetic energy and/or momentum to the atoms arriving at the film surface) has been extensively studied and constitutes the basis of the well-known structure zone diagrams (SZDs) [52–56]. However, reports dealing with the microstructural tuning of sputter-deposited metallic glass thin films are much scarcer [25]. Glassy films deposited by sputtering exhibit three growth modes depending on the surface diffusivity of adatoms on the substrate [36–38,40,41,57]. Homogeneous and compact films, with a smooth surface, have been obtained at high adatom surface diffusivity. Films presenting a nanocolumnar microstructure, with the top of the columns in the form of a dome, have been obtained at low adatom surface diffusivity. Finally, a third growth mode at intermediate values of adatom surface diffusivity has been reported, leading to the formation of films which are homogeneous and compact in cross-section, but present a nanogranular and non-smooth surface. As seen in Fig. 2, the three growth modes were also found here in the

case of the Zr-Cu system. They can be observed, for example, with the increase of working pressure and the consequent decrease of surface diffusivity of the adatoms for the 65 at.% Cu films.

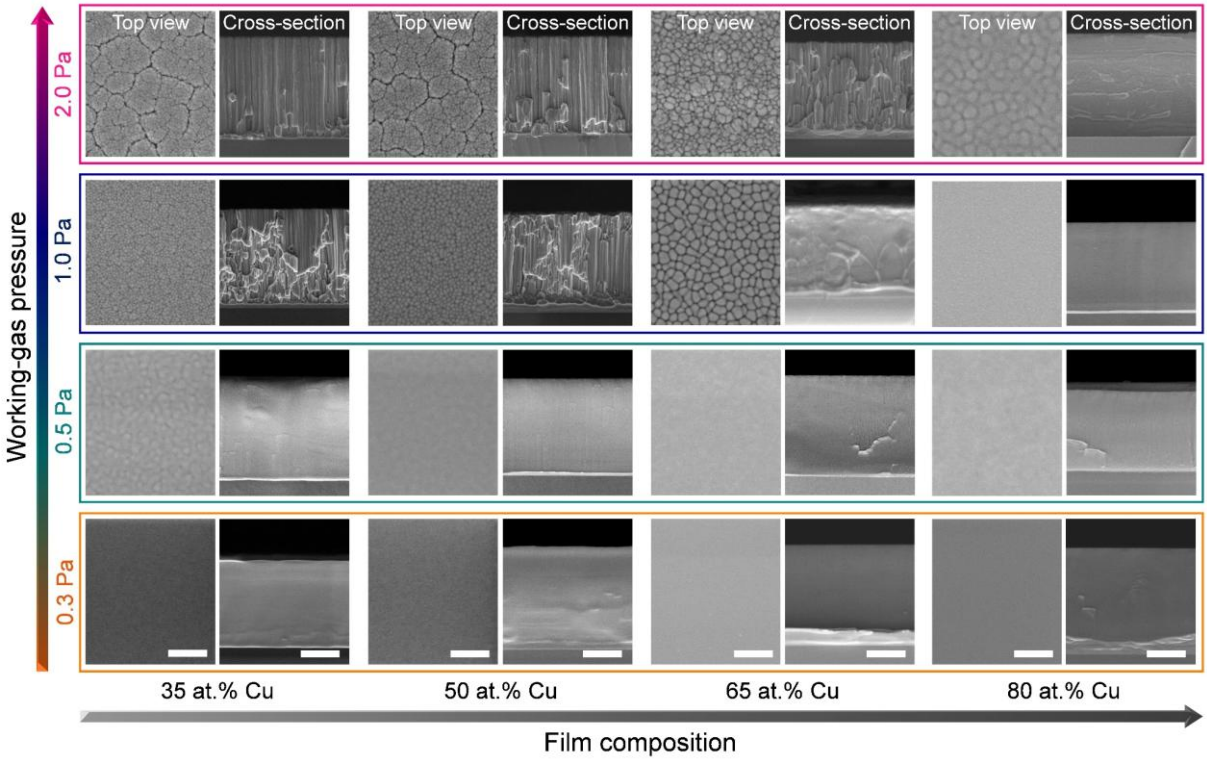

Figure 2. Pressure-composition mapping of morphology variation in Zr-Cu thin film metallic glasses. The top and cross-section view SEM images show that the microstructure of the films evolves from homogeneous to nanocolumnar by either increasing the working pressure or decreasing the Cu content. Scale bar of top and cross-section views: 200 and 400 nm, respectively.

The microstructural difference between the growth modes has been explained as being due to a competition between the shadowing effect and the surface diffusivity of the adatoms [38]. The shadowing effect, which consists in the higher probability of atoms arriving at the substrate from multiple directions to land preferentially on top of a hill than in a valley, induces the formation of columns terminated by a dome at the top. Nevertheless, if the surface diffusivity of adatoms is high enough, they can diffuse from the top of columns to the boundary between them, and also smoothen the surface, resulting in the formation of compact and homogeneous films with featureless top views. For intermediate values of surface

diffusivity, the adatoms exhibit sufficient mobility to diffuse in between the columns, which prevent the formation of voided boundaries, but not enough mobility to smoothen the dome-shaped column tops, creating a granular appearance of the film surface. We note that the size of surface "grains" for films obtained at intermediate values of adatom surface diffusivity is larger than the column width of columnar films (see, for example, 65 at.% Cu films deposited at 1.0 and 2.0 Pa). This is in line with the fact that columnar films are obtained at lower values of surface diffusivity, inhibiting the initial lateral growth of the columns.

The transition from a homogeneous to a nanocolumnar microstructure has been reported in glassy Ni-Nb films by either increasing the working pressure [36] or decreasing the substrate temperature [41], which, in both cases, limits the surface diffusivity of the adatoms. Similarly, in Ni-Ti [40], TiZrCuPd [37], Au-based and Zr-based [38] metallic glass thin films the homogeneous to nanocolumnar transition has been detected with increasing working-gas pressure. We point out that in the Zr-Cu system, the three growth modes have been reported by different authors: homogeneous [58], columnar [59,60,43,61] and nanogranular from top view [62–65], but there is no study on the possibility of microstructural manipulation in this system, which is at the core of the present work.

The wide range of alloy compositions and working pressures explored in this study sheds light on an interesting point: the impact of the chemical composition on the transition from homogeneous to nanocolumnar growth modes. As evidenced by Fig. 2, with increasing Cu content, the transition from homogeneous to nanostructured films occurred at higher working pressure. For example, 35 at.% Cu films deposited at 1.0 Pa present a nanocolumnar microstructure, typical of a low surface diffusivity of adatoms, whereas 80 at.% Cu films obtained at the same pressure (1.0 Pa) exhibit a smooth surface with a homogeneous microstructure, which corresponds to high values of adatoms surface diffusivity. At this composition, it was necessary to increase the working pressure to 2.0 Pa to detect a change in

the surface morphology of the films. This shift with composition of the transition between growth modes can be understood by considering the difference in the surface diffusivity of the chemical species forming the alloy. If one of the species composing the alloy have a higher surface diffusivity compared to the others, films richer in the more mobile specie will exhibit a higher overall surface diffusivity compared to films with lower contents of the more mobile specie. Thus, a higher surface diffusivity of Cu adatoms compared to the Zr ones would explain that in Cu-rich films the transition from a homogeneous to a nanocolumnar microstructure shift towards higher working pressures. There are several factors that support a higher surface diffusivity of Cu adatoms. First, the smaller size of Cu (atomic radius = 0.126 nm) compared with Zr (atomic radius = 0.158 nm) [66], which acts in favor of the diffusivity of adatoms on the film surface. Second, the melting temperature of Cu (T_m = 1358 K) is much lower than that of Zr (T_m = 2128 K) [67]. Thus, the homologous temperature of Cu ($T_h = T_s/T_m$ = 0.22), defined as the ratio between the substrate temperature (T_s = 300 K) and the melting temperature, is higher than the one of Zr (T_h = 0.14). The homologous temperature is a crucial parameter used to classify the microstructure in the SZDs, constituting a measure of the adatoms surface mobility in vapor-deposited films [52–56,68]. Finally, molecular dynamics simulations have shown that in $Zr_{50}Cu_{50}$ alloy the diffusion coefficient of Cu is higher than that of Zr [69,70].

3.2. Impact of microstructure on the local order of Zr-Cu thin film metallic glasses

As previously noted by TEM analysis (Fig. 1d), Δq increased with the microstructural transition from homogeneous to nanocolumnar, indicating a change in the local order of the films. X-ray diffraction analysis provided details on this regard (Fig. 3 and Fig. S2, Supplementary Information). At first sight, the X-ray diffractograms of films deposited at 0.3 and 2.0 Pa appear similar. The first diffraction peak is shifted towards higher values with increasing Cu content. Moreover, the peak width, determined as the full-width at half-maximum (Δq), gradually decreases upon changes in composition from ~50 at.% Cu towards the Zr-rich and Cu-rich sides (Fig. 3a). This behavior is in line with previous reports on this system [51,58,61,62,71]. However, a quantitative analysis of the X-ray diffractograms disclosed that the evolution of Δq with alloy composition depends, in fact, on the working-gas pressure at which the films were deposited (Fig. 3b). Similar to what was observed by TEM analysis, Δq presented a general tendency to increase with increasing working pressure.

To determine whether a film presents an amorphous (indicated by circles) or crystalline (indicated by triangles) structure, we used the following criteria: first, the sample does not exhibit a sharp peak in the X-ray diffractograms and, second, the Δq is larger than 0.25 $Å^{-1}$ [72]. This threshold results in correlation lengths, estimated as $L = 2\pi/\Delta q$ [48], of less than 25 Å for all amorphous films (see Fig. S3, Supplementary Information). We point out that, although the evolution of Δq with Cu content was affected by the working pressure, the amorphous-forming composition range (AFCR) of the films did not show a strong variation. The transition from films with an amorphous phase to films with a crystalline phase occurred at approx. 87 at.% Cu on the Cu-rich side, and was not impacted by the working pressure. On the Zr-rich side, the phase transition shifted slightly from approx. 21 to 18 at.% Cu with increasing working pressure from 0.3 to 2.0 Pa (Fig. 2b and Fig. S4, Supplementary Information). Such a wide AFCR (from approx. 20 to 87 at.% Cu) is in line with that reported

by Zeman *et al.* [58] and Brognara *et al.* [61] on sputter-deposited Zr-Cu films. Using molecular dynamics simulations, Houska *et al.* [73] found a similar AFCR. In addition, the authors showed that the AFCR is not strongly affected by the energy of atoms arriving to the substrate [73]. Interestingly, this AFCR is extremely close to that predicted by the simplistic Egami and Waseda model (AFCR from 21 to 87 at.% Cu) [74], which is based solely on the atomic size differences of the chemical elements forming the alloy. We also note that some authors have reported the formation of a crystalline phase up to ~30 at.% Cu, as in the case of Apreutesei *et al.* [62] and You *et al.* [72].

To further investigate the effect of microstructure on Δq, we analyzed SEM images with the aim of associating Δq with the growth mode of the films: homogeneous with smooth surface, compact but nanogranular from the top, and nanocolumnar (Fig. 3c). We found that, for a given alloy composition, Δq increases if the working pressure is such that the surface diffusivity of the adatoms is sufficiently limited to transition to a nanocolumnar microstructure. Note that the dependence between Δq and Cu content is not affected as long as the films are deposited under conditions of high or intermediate values of adatom surface diffusivity, for which the microstructure is homogeneous, with either a smooth or nanogranular surface. This result highlights the impact that the creation of interfaces, due to the transition to the nanocolumnar regime, has on the increase of Δq.

To explain this behavior, we can rely on the interpretation of Δq given by Li *et al.* [48]. In their work, the authors demonstrated a correlation between large Δq values and high GFA. They associated this correlation to the fact that larger Δq values are due to a higher number of different polyhedral types (or structural units) forming the amorphous structure (this is because the atomic distances within each structural unit differ from each other). Meanwhile, a higher number of involved polyhedral types results in more efficient space filling and dense atomic packing of the amorphous phase which, in turn, favors the GFA. Therefore, the Δq-

GFA correlation arises from the fact that Δq constitutes a measurement of the dispersity of the structural units comprising the amorphous structure [48]. In line with this correlation, in Zr-Cu alloys, Δq reaches a maximum at ~50 at.% Cu (Fig. 3b) which is known to be one of the compositions with the best GFA in this system [44,75]. Hence, the increase in Δq reported herein indicates that the transition to the nanocolumnar growth mode induces an increase in the number of structural units forming the amorphous phase. This can be understood considering that the atoms at the interfaces between the formed nanocolumns do not have the same dynamics as the atoms in the interior (bulk) of the nanocolumns, mainly because the mobility of surface atoms is higher than that of atoms in the bulk [70]. Such a broad difference in the mobility of atoms in the nanocolumnar regime compared to the homogeneous regime, where most of the atoms are in the bulk of the film, can promote the formation of more polyhedral types, favoring the increase of Δq.

In contrast to Δq, the change in growth mode with increasing working pressure does not affect the peak position, q (Fig. 3d). In general, q is inversely proportional to the average interatomic nearest-neighbor distance, d ($q \sim 1/d$) [76–79]. Therefore, our results indicate that although transition to the nanocolumnar regime increases the number of different polyhedral types, it does not impact the average nearest-neighbor distance. We can also observe that the variation of q with Cu content follows the behavior reported in ribbons [51] and that obtained by molecular dynamic simulation [80], pointing to the conclusion that the change in q value with composition is intrinsic to the alloy system and that it does not depend on the synthesis method. We note that the dependence of q on alloy composition is not linear, but deviates slightly from the linear interpolation between the (111) planes of the fcc phase of Zr and Cu (Fig. 3d).

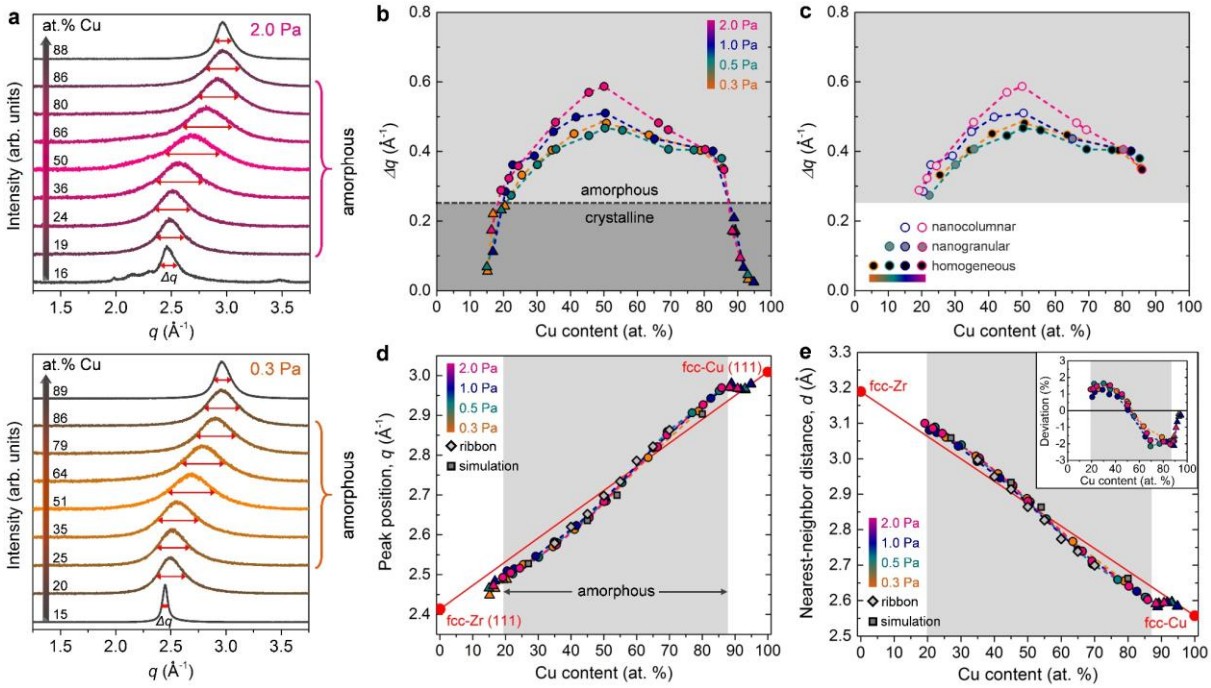

Figure 3. Structural characterization of nanostructured Zr-Cu films by X-ray diffraction analysis. (a) X-ray diffractograms of Zr-Cu alloys deposited at 0.3 Pa (bottom) and 2.0 Pa (top) showing the change in the peak position and the full-width at half-maximum, Δq, with the film composition. (b) Plot of Δq as a function of Cu content of films deposited at 0.3, 0.5, 1.0 and 2.0 Pa. A threshold of Δq = 0.25 Å^{-1} was used to separate amorphous from crystalline films. (c) Evolution of Δq versus Cu content at different working pressures showing the growth mode in which the films were deposited: homogeneous with smooth surface, compact but nanogranular on top, and nanocolumnar. (d) Variation of the peak position, q, with Cu content at different working pressures. Values reported in ribbons (extracted from [51]) and that obtained by molecular dynamic simulation (extracted from [80]) are also shown with light-gray diamonds and dark-gray squares, respectively. The red line follows a linear interpolation between the (111) planes of the fcc phase of Zr and Cu. (e) Average nearest-neighbor distance estimated using Ehrenfest equation for the amorphous samples. In the case of crystalline samples in the Cu-rich side, the nearest-neighbor distance was determined by assuming that the first X-ray diffraction peak corresponds to the reflection of the (111) planes of the fcc phase of Cu. The red line follows the mixing law between pure fcc Zr and Cu (indicated with red circles). The inset shows the deviation of d from the mixing law. In (b), (c), (d) and (e) amorphous samples are indicated by circles and crystalline samples by triangles. The light gray area in (d) and (e) serves as a guide for the eyes to indicate the range of compositions for the formation of amorphous films.

To gain insight into the meaning of this deviation from linear behavior, we roughly estimated the average nearest-neighbor distance of atoms in the amorphous phase by using Ehrenfest equation, $d_{amorph} = 1.23 \times 2\pi/q$ [58,78]. We also determined the nearest-neighbor distance for the crystalline samples in the Cu-riche side by assuming that the first X-ray diffraction peak corresponds to the reflection of the (111) planes of the fcc phase of Cu, $d_{cryst} = \sqrt{6}/2 \times 2\pi/q$. In Fig. 3e, we compare the calculated d values with the expected nearest-neighbor distance evaluated from the mixing law applied to pure fcc Zr and Cu (red line). We can notice that the variation of the calculated values of d with Cu content is not linear and deviates from the values expected using the mixing law (inset in Fig. 3e). This differs from the often reported linearity [58,62], which may be due to the relatively sparse data points in previous studies. With increasing Cu content, the average nearest-neighbor distance decreases, in line with the smaller atomic radius of Cu compared to Zr. In addition, at ~50 at.% Cu, d turns from being higher to being lower than expected by the mixing law. Similar behavior has also been reported by Coddet *et al.* [71]. The faster decrease in the average nearest-neighbor distance of the amorphous films compared to the distance expected from the mixture law (inset in Fig. 3e) indicates an increase in atomic packing density with increasing Cu content up to ~70 at.%, in line with previously published results on Zr-Cu alloys [73,81]. We point-out that residual stresses in the films can be disregarded as the cause of the deviation from the linear behavior of the peak position (or average nearest-neighbor distance) herein reported. This is supported by the fact that residual stress measurements performed to the films showed a compressive-to-tensile transition with increasing working pressure (Fig. S5, Supplementary Information). However, at a fixed composition, the value of q (Fig. 3d) is not affected by this change in residual stress, evidencing the negligible impact of residual stresses on the peak position.

3.3. Tailored electrical and optical properties of nanostructured Zr-Cu metallic glass thin films

The microstructural change herein demonstrated in glassy Zr-Cu alloys, triggered by increasing working-gas pressure, had a significant impact on the electrical and optical properties of the films. Fig. 4a shows the effect of working pressure on the electrical resistivity of the films. Similar to the behavior of Δq, for a given alloy composition, the electrical resistivity increases with working pressure once the working pressure is such that the microstructure of the films transitions to the nanocolumnar regime (Fig. S6a, Supplementary Information). We can also see that, as long as the microstructure remains homogeneous (with a smooth or nanogranular surface), the resistivity follows the same behavior as reported for ribbon samples [82]. The increase in resistivity can be associated with the formation of boundaries between nanocolumns, which are voided or lower density regions and, consequently, exhibit lower electrical conductivity. The optical reflectance of the films is also affected by the working pressure (Fig. 4b and Fig. S7, Supplementary Information). In Fig. 4b is shown the variation of the total reflectance measured at a wavelength of 2500 nm (near-infrared region). In agreement with the results obtained for Δq and resistivity, the reflectance of the films can be tailored once their microstructure transitions to the nanocolumnar regime (Fig. S6b, Supplementary Information).

The electrical resistivity and optical reflectance showed opposite trends with increasing working pressure, i.e., resistivity increased while reflectance decreased (Fig. 4a-b). This is also illustrated in Fig. 4c, which highlights the impact of alloy composition on the change of resistivity and reflectance with working pressure. As the Cu content is increased, the variation of resistivity and reflectance became less pronounced. In $Zr_{50}Cu_{50}$ films, an increase in working pressure from 0.3 to 2.0 Pa resulted in a change in resistivity from 180 to 899 μΩ cm (a 400% increase) and a change in reflectance from 0.77 to 0.58 (a 25% decrease). However,

in $Zr_{20}Cu_{80}$ films the same increase in working pressure does not induce a noticeable change in resistivity or reflectance. These results are in line with the shift to higher working pressure, with increasing Cu content, of the homogeneous to nanocolumnar microstructural transition. We also note the existence of a threshold in the working pressure (~ 0.5 Pa in our case) below which the resistivity and reflectance no longer change, whatever the alloy composition.

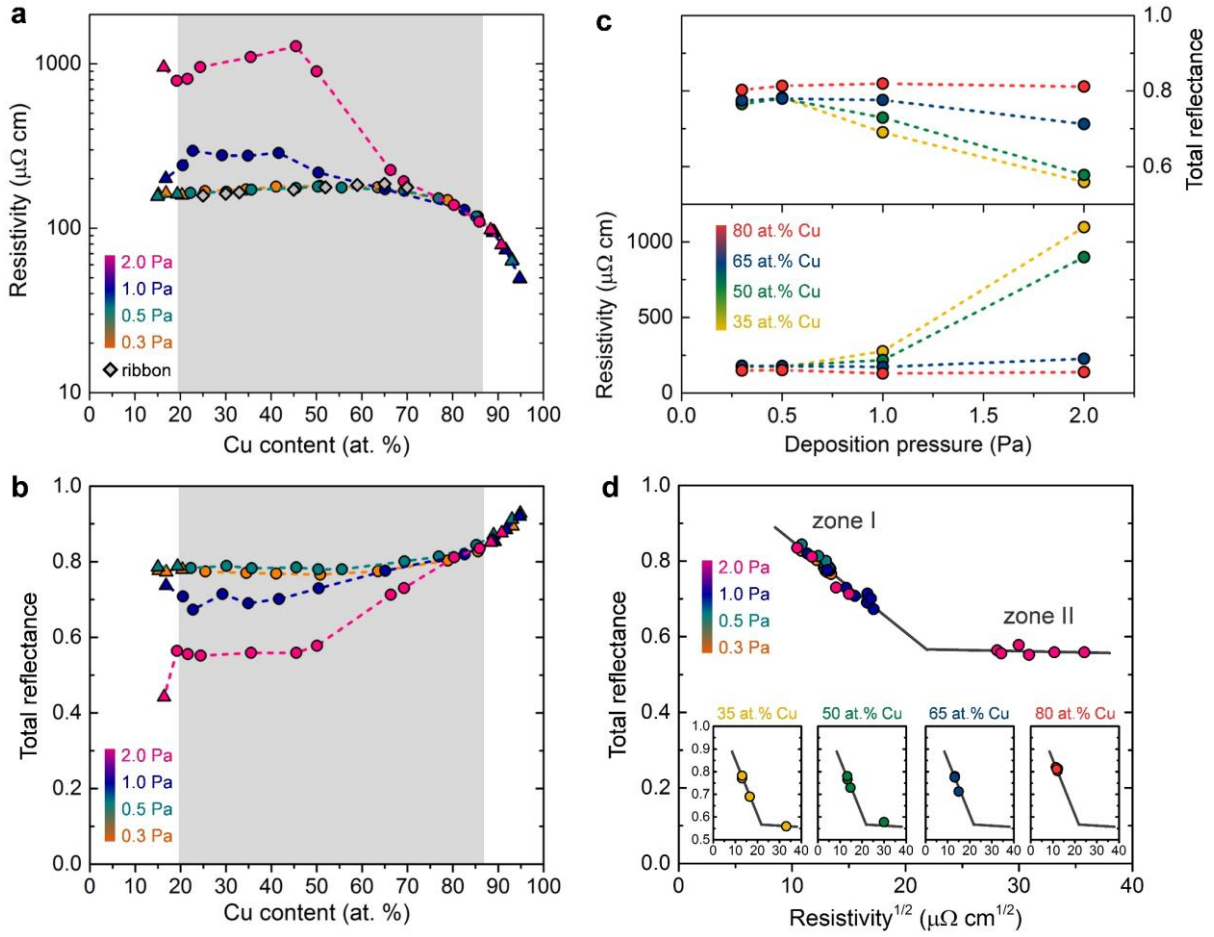

Figure 4. Tailored electrical and optical properties of nanostructured Zr-Cu films. Electrical resistivity (a) and optical reflectance (b) versus alloy composition of films deposited at 0.3, 0.5, 1.0 and 2.0 Pa. Amorphous samples are indicated by circles and crystalline samples by triangles. The light gray area serves as a guide for the eyes to indicate the range of compositions for the formation of amorphous films. In (a), the resistivity of ribbon samples (extracted from [82]) is shown with gray diamonds. (c) Variation of resistivity and reflectance with working-gas pressure of films with 35, 50, 65 and 80 at.% Cu. (d) Plot of the reflectance versus the square root of resistivity for the alloys marked as amorphous. The insets show this dependence for films with 35, 50, 65 and 80 at.% Cu.

The opposite trend of electrical resistivity, ρ, and optical reflectance, R, can be explained using the free electron model for metals [83,84]. Assuming $n << k$ (n and k are the real and imaginary parts of the refractive index, respectively), the reflectance can be related to the resistivity as [83,84]:

$$R \approx 1 - A\rho^{1/2}, \qquad (1)$$

where A is a proportional constant. The assumed condition $n << k$ is valid for most metals in the near-infrared wavelength region. For example, for Cu, n = 0.5 and k = 17.9 at a wavelength of 2500 nm [85]. The inverse relationship between reflectance and resistivity expressed through Eq. 1 has being previously reported in other glassy systems such as Ag-Mg-Al [83,86], Al-Ni-Y-X (X = Cu, Ta, Zr) [87], and Al-Ti [84] alloys. Fig. 4d shows the dependence of reflectance versus the square root of resistivity for amorphous Zr-Cu films. We identified two zones: a first one, for $\rho^{1/2} < 20$ ($\mu\Omega$ cm)$^{1/2}$ (or $\rho < 400$ $\mu\Omega$ cm), in which the free electron model relation for $n << k$ is fulfilled, and a second one, for $\rho^{1/2} > 20$ ($\mu\Omega$ cm)$^{1/2}$ (or $\rho > 400$ $\mu\Omega$ cm), in which the reflectance no longer depends on the resistivity. As a matter of fact, in zone 1, the best fit to the experimental data follows the relation:

$$R = 1.095 - 0.024\,\rho^{1/2}, \qquad (2)$$

in good agreement with Eq. 1, whereas in zone 2 the reflectance $R \approx 0.57$, with a negligible slope of the R versus $\rho^{1/2}$ relation. The deviation from Eq. 1 at high resistivity values ($\rho > 400$ $\mu\Omega$ cm) is presumably due to the violation of the condition $n << k$ in amorphous films exhibiting such high values of resistivity. This can be attributed to the fact that high resistivity values are achieved in films presenting a high number of less dense and conductive interfacial regions between the nanocolumns, which implies a loss of the metallic character of the whole film, necessary to fulfill Eq. 1.

We dedicate a last point to comment on the tunability of electrical resistivity and optical reflectance in glassy Zr-Cu alloys. We note that, whatever the alloy composition, low resistivity films (zone 1) follow the same scaling law (expressed through Eq. 2), whereas the terminal reflectance is the same ($R \approx 0.57$) for high resistivity films (zone 2). This is illustrated in the insets of Fig. 4d showing the variation of R versus $\rho^{1/2}$ for the 35, 50, 65 and 80 at.% Cu films. Therefore, our results indicate that even in alloys of different compositions, resistivity and reflectance can be tailored following the same law. The difference between alloys with different compositions is that the higher the Cu content, the higher the working pressure needed to tailor the reflectance and resistivity of the films.

4. Conclusions

In summary, we identified the conditions for the formation of nanostructured Zr-Cu metallic glass thin films and the consequent impact on the electrical resistivity and optical reflectance of the alloys. For this purpose, we investigated over a wide range of alloy composition (from ~16 to 94 at.% Cu) and working-gas pressure (from 0.3 to 2 Pa) the evolution of the structure, microstructure, resistivity and reflectance of sputter-deposited Zr-Cu films. We demonstrated that, by increasing the working pressure, the microstructure of the amorphous films transitions from homogeneous and compact to nanocolumnar. However, this change in microstructure shifts towards higher working pressure with increasing Cu content, which was explained considering the difference in the surface diffusivity of Cu adatoms compared to Zr ones. We also showed that the microstructural transition to the nanocolumnar regime causes an increase in the full-width at half-maximum, Δq, of the first diffraction peak in the diffraction pattern, suggesting a change in the local order of the films induced by an increase in the number of different structural units forming the amorphous phase. In contrast to Δq, the microstructural change did not affect the position of the peak, q, indicating that it did not impact the average interatomic nearest-neighbor distance. Regarding the electrical and optical properties of

glassy Zr-Cu films, two zones were identified, one in which the optical reflectance scales linearly with the square root of the electrical resistivity, and another in which reflectance no longer depends on resistivity. We highlighted that, by increasing the working pressure, the resistivity and reflectance can be tailored starting from their values in the homogeneous regime and following the same scaling law, whatever the alloy composition. Our results provide a step forward in understanding the microstructural control of metallic glass thin films and shed light on the modulation of electrical and optical properties in glassy alloys, which could have implications for optoelectronic applications.

Declaration of Competing Interest

The authors declare that they have no known competing financial interests or personal relationships that could have appeared to influence the work reported in this paper.

Acknowledgements

This work was supported by the ANR project MEGALIT (ANR-18-CE08-0018) of the French Agence Nationale de la Recherche. The Daυm competence center of IJL is deeply acknowledged for access to UHV magnetron sputtering deposition facility.

References

[1] H. Van Swygenhoven, Grain Boundaries and Dislocations, Science. 296 (2002) 66–67. https://doi.org/10.1126/science.1071040.
[2] T. Watanabe, Grain boundary engineering: historical perspective and future prospects, J Mater Sci. 46 (2011) 4095–4115. https://doi.org/10.1007/s10853-011-5393-z.
[3] Z. Chen, Z. Jian, W. Li, Y. Chang, B. Ge, R. Hanus, J. Yang, Y. Chen, M. Huang, G.J. Snyder, Y. Pei, Lattice Dislocations Enhancing Thermoelectric PbTe in Addition to Band Convergence, Advanced Materials. 29 (2017) 1606768. https://doi.org/10.1002/adma.201606768.
[4] A.-F. Castro-Méndez, J. Hidalgo, J.-P. Correa-Baena, The Role of Grain Boundaries in Perovskite Solar Cells, Advanced Energy Materials. 9 (2019) 1901489. https://doi.org/10.1002/aenm.201901489.
[5] M. Wang, B.B. He, M.X. Huang, Strong and ductile Mg alloys developed by dislocation engineering, Journal of Materials Science & Technology. 35 (2019) 394–395. https://doi.org/10.1016/j.jmst.2018.09.033.

[6] H. Gleiter, Nanocrystalline materials, Progress in Materials Science. 33 (1989) 223–315. https://doi.org/10.1016/0079-6425(89)90001-7.
[7] H. Gleiter, J. Weissmüller, O. Wollersheim, R. Würschum, Nanocrystalline materials: a way to solids with tunable electronic structures and properties?, Acta Materialia. 49 (2001) 737–745. https://doi.org/10.1016/S1359-6454(00)00221-4.
[8] C. Suryanarayana, The structure and properties of nanocrystalline materials: Issues and concerns, JOM. 54 (2002) 24–27. https://doi.org/10.1007/BF02709088.
[9] M.A. Meyers, A. Mishra, D.J. Benson, Mechanical properties of nanocrystalline materials, Progress in Materials Science. 51 (2006) 427–556. https://doi.org/10.1016/j.pmatsci.2005.08.003.
[10] T.J. Rupert, J.C. Trenkle, C.A. Schuh, Enhanced solid solution effects on the strength of nanocrystalline alloys, Acta Materialia. 59 (2011) 1619–1631. https://doi.org/10.1016/j.actamat.2010.11.026.
[11] J. Jing, A. Krämer, R. Birringer, H. Gleiter, U. Gonser, Modified atomic structure in a Pd-Fe-Si nanoglass: A Mössbauer study, Journal of Non-Crystalline Solids. 113 (1989) 167–170. https://doi.org/10.1016/0022-3093(89)90007-0.
[12] H. Gleiter, Our thoughts are ours, their ends none of our own: Are there ways to synthesize materials beyond the limitations of today?, Acta Materialia. 56 (2008) 5875–5893. https://doi.org/10.1016/j.actamat.2008.08.028.
[13] J.X. Fang, U. Vainio, W. Puff, R. Würschum, X.L. Wang, D. Wang, M. Ghafari, F. Jiang, J. Sun, H. Hahn, H. Gleiter, Atomic Structure and Structural Stability of Sc75Fe25 Nanoglasses, Nano Lett. 12 (2012) 458–463. https://doi.org/10.1021/nl2038216.
[14] M. Ghafari, H. Hahn, H. Gleiter, Y. Sakurai, M. Itou, S. Kamali, Evidence of itinerant magnetism in a metallic nanoglass, Appl. Phys. Lett. 101 (2012) 243104. https://doi.org/10.1063/1.4769816.
[15] R. Witte, T. Feng, J.X. Fang, A. Fischer, M. Ghafari, R. Kruk, R.A. Brand, D. Wang, H. Hahn, H. Gleiter, Evidence for enhanced ferromagnetism in an iron-based nanoglass, Appl. Phys. Lett. 103 (2013) 073106. https://doi.org/10.1063/1.4818493.
[16] H. Gleiter, Nanoglasses: a new kind of noncrystalline materials, Beilstein J. Nanotechnol. 4 (2013) 517–533. https://doi.org/10.3762/bjnano.4.61.
[17] H. Gleiter, Th. Schimmel, H. Hahn, Nanostructured solids – From nano-glasses to quantum transistors, Nano Today. 9 (2014) 17–68. https://doi.org/10.1016/j.nantod.2014.02.008.
[18] D. Danilov, H. Hahn, H. Gleiter, W. Wenzel, Mechanisms of Nanoglass Ultrastability, ACS Nano. 10 (2016) 3241–3247. https://doi.org/10.1021/acsnano.5b05897.
[19] H. Gleiter, Nanoglasses: A New Kind of Noncrystalline Material and the Way to an Age of New Technologies?, Small. 12 (2016) 2225–2233. https://doi.org/10.1002/smll.201500899.
[20] Q. Hu, J. Wu, B. Zhang, Synthesis and nanoindentation behaviors of binary CuTi nanoglass films, Physica B: Condensed Matter. 521 (2017) 28–31. https://doi.org/10.1016/j.physb.2017.06.053.
[21] M.R. Chellali, S.H. Nandam, S. Li, M.H. Fawey, E. Moreno-Pineda, L. Velasco, T. Boll, L. Pastewka, R. Kruk, P. Gumbsch, H. Hahn, Amorphous nickel nanophases inducing ferromagnetism in equiatomic NiTi alloy, Acta Materialia. 161 (2018) 47–53. https://doi.org/10.1016/j.actamat.2018.09.019.
[22] A. Baksi, S.H. Nandam, D. Wang, R. Kruk, M.R. Chellali, J. Ivanisenko, I. Gallino, H. Hahn, S. Bag, Ni60Nb40 Nanoglass for Tunable Magnetism and Methanol Oxidation, ACS Appl. Nano Mater. 3 (2020) 7252–7259. https://doi.org/10.1021/acsanm.0c01584.

[23] N. Chen, D.V. Louzguine-Luzgin, K. Yao, A new class of non-crystalline materials: Nanogranular metallic glasses, Journal of Alloys and Compounds. 707 (2017) 371–378. https://doi.org/10.1016/j.jallcom.2016.11.304.
[24] Y. Ivanisenko, C. Kübel, S.H. Nandam, C. Wang, X. Mu, O. Adjaoud, K. Albe, H. Hahn, Structure and Properties of Nanoglasses, Advanced Engineering Materials. 20 (2018) 1800404. https://doi.org/10.1002/adem.201800404.
[25] Q.P. Cao, L.B. Lv, X.D. Wang, J.Z. Jiang, H.-J. Fecht, Synthesis and properties optimization of high-performance nanostructured metallic glass thin films, Materials Today Nano. 14 (2021) 100114. https://doi.org/10.1016/j.mtnano.2021.100114.
[26] A. Kartouzian, Cluster-assembled metallic glasses, Nanoscale Research Letters. 8 (2013) 339. https://doi.org/10.1186/1556-276X-8-339.
[27] A. Kartouzian, J. Antonowicz, T. Lünskens, A. Lagogianni, P. Heister, G. Evangelakis, R. Felici, Toward cluster-assembled metallic glasses, Materials Express. 4 (2014) 228–234. https://doi.org/10.1166/mex.2014.1168.
[28] C. Benel, A. Fischer, A. Zimina, R. Steininger, R. Kruk, H. Hahn, A. Léon, Controlling the structure and magnetic properties of cluster-assembled metallic glasses, Materials Horizons. 6 (2019) 727–732. https://doi.org/10.1039/C8MH01013G.
[29] S.P. Chilakalapudi, S. Katnagallu, A. Sarkar, P. Cao, W. Wenzel, H. Hahn, Energetically deposited cluster assembly of metallic glasses, Acta Materialia. 237 (2022) 118152. https://doi.org/10.1016/j.actamat.2022.118152.
[30] N. Chen, R. Frank, N. Asao, D.V. Louzguine-Luzgin, P. Sharma, J.Q. Wang, G.Q. Xie, Y. Ishikawa, N. Hatakeyama, Y.C. Lin, M. Esashi, Y. Yamamoto, A. Inoue, Formation and properties of Au-based nanograined metallic glasses, Acta Materialia. 59 (2011) 6433–6440. https://doi.org/10.1016/j.actamat.2011.07.007.
[31] N. Chen, D.V. Louzguine-Luzgin, G.Q. Xie, P. Sharma, J.H. Perepezko, M. Esashi, A.R. Yavari, A. Inoue, Structural investigation and mechanical properties of a representative of a new class of materials: nanograined metallic glasses, Nanotechnology. 24 (2013) 045610. https://doi.org/10.1088/0957-4484/24/4/045610.
[32] N. Chen, X. Shi, R. Witte, K.S. Nakayama, K. Ohmura, H. Wu, A. Takeuchi, H. Hahn, M. Esashi, H. Gleiter, A. Inoue, D.V. Louzguine, A novel Ti-based nanoglass composite with submicron–nanometer-sized hierarchical structures to modulate osteoblast behaviors, J. Mater. Chem. B. 1 (2013) 2568–2574. https://doi.org/10.1039/C3TB20153H.
[33] J.Q. Wang, N. Chen, P. Liu, Z. Wang, D.V. Louzguine-Luzgin, M.W. Chen, J.H. Perepezko, The ultrastable kinetic behavior of an Au-based nanoglass, Acta Materialia. 79 (2014) 30–36. https://doi.org/10.1016/j.actamat.2014.07.015.
[34] S.V. Ketov, X. Shi, G. Xie, R. Kumashiro, A.Yu. Churyumov, A.I. Bazlov, N. Chen, Y. Ishikawa, N. Asao, H. Wu, D.V. Louzguine-Luzgin, Nanostructured Zr-Pd Metallic Glass Thin Film for Biochemical Applications, Sci Rep. 5 (2015) 7799. https://doi.org/10.1038/srep07799.
[35] Z. Śniadecki, D. Wang, Yu. Ivanisenko, V.S.K. Chakravadhanula, C. Kübel, H. Hahn, H. Gleiter, Nanoscale morphology of Ni50Ti45Cu5 nanoglass, Materials Characterization. 113 (2016) 26–33. https://doi.org/10.1016/j.matchar.2015.12.025.
[36] S.V. Ketov, R. Joksimovic, G. Xie, A. Trifonov, K. Kurihara, D.V. Louzguine-Luzgin, Formation of nanostructured metallic glass thin films upon sputtering, Heliyon. 3 (2017) e00228. https://doi.org/10.1016/j.heliyon.2016.e00228.
[37] M. Mohri, D. Wang, J. Ivanisenko, H. Gleiter, H. Hahn, Investigation of the deposition conditions on the microstructure of TiZrCuPd nano-glass thin films, Materials Characterization. 131 (2017) 140–147. https://doi.org/10.1016/j.matchar.2017.07.014.

[38] P. Denis, S.Y. Liu, H.-J. Fecht, Growth mode transition in Au-based thin film metallic glasses, Thin Solid Films. 665 (2018) 29–35. https://doi.org/10.1016/j.tsf.2018.08.006.
[39] A. Rauf, Y. Fang, H. Zhang, G. Peng, T. Feng, Thickness effects on microstructure, mechanical and soft magnetic properties of sputtered Fe Zr thin film metallic glass, Journal of Non-Crystalline Solids. 521 (2019) 119500. https://doi.org/10.1016/j.jnoncrysol.2019.119500.
[40] M. Mohri, M. Nili-Ahmadabadi, On the nano-glass formation of the Ni–Ti thin films and related micro-structure and mechanical properties by controlling sputtering conditions, Mater. Res. Express. 6 (2019) 076421. https://doi.org/10.1088/2053-1591/ab0c37.
[41] W. Yao, Q.P. Cao, S.Y. Liu, X.D. Wang, H.J. Fecht, A. Caron, D.X. Zhang, J.Z. Jiang, Tailoring nanostructured Ni-Nb metallic glassy thin films by substrate temperature, Acta Materialia. 194 (2020) 13–26. https://doi.org/10.1016/j.actamat.2020.04.046.
[42] M. Prudent, F. Bourquard, A. Borroto, J.-F. Pierson, F. Garrelie, J.-P. Colombier, Initial Morphology and Feedback Effects on Laser-Induced Periodic Nanostructuring of Thin-Film Metallic Glasses, Nanomaterials. 11 (2021) 1076. https://doi.org/10.3390/nano11051076.
[43] M. Prudent, D. Iabbaden, F. Bourquard, S. Reynaud, Y. Lefkir, A. Borroto, J.-F. Pierson, F. Garrelie, J.-P. Colombier, High-Density Nanowells Formation in Ultrafast Laser-Irradiated Thin Film Metallic Glass, Nano-Micro Lett. 14 (2022) 103. https://doi.org/10.1007/s40820-022-00850-4.
[44] Y. Li, Q. Guo, J.A. Kalb, C.V. Thompson, Matching Glass-Forming Ability with the Density of the Amorphous Phase, Science. 322 (2008) 1816–1819. https://doi.org/10.1126/science.1163062.
[45] O. Adjaoud, K. Albe, Interfaces and interphases in nanoglasses: Surface segregation effects and their implications on structural properties, Acta Materialia. 113 (2016) 284–292. https://doi.org/10.1016/j.actamat.2016.05.002.
[46] S.H. Nandam, Y. Ivanisenko, R. Schwaiger, Z. Śniadecki, X. Mu, D. Wang, R. Chellali, T. Boll, A. Kilmametov, T. Bergfeldt, H. Gleiter, H. Hahn, Cu-Zr nanoglasses: Atomic structure, thermal stability and indentation properties, Acta Materialia. 136 (2017) 181–189. https://doi.org/10.1016/j.actamat.201.07.001.
[47] K. Zheng, S. Yuan, H. Hahn, P.S. Branicio, Excess free volume and structural properties of inert gas condensation synthesized nanoparticles based CuZr nanoglasses, Sci Rep. 11 (2021) 19246. https://doi.org/10.1038/s41598-021-98494-8.
[48] M.-X. Li, Y.-T. Sun, C. Wang, L.-W. Hu, S. Sohn, J. Schroers, W.-H. Wang, Y.-H. Liu, Data-driven discovery of a universal indicator for metallic glass forming ability, Nat. Mater. (2021). https://doi.org/10.1038/s41563-021-01129-6.
[49] G.C.A.M. Janssen, M.M. Abdalla, F. van Keulen, B.R. Pujada, B. van Venrooy, Celebrating the 100th anniversary of the Stoney equation for film stress: Developments from polycrystalline steel strips to single crystal silicon wafers, Thin Solid Films. 517 (2009) 1858–1867. https://doi.org/10.1016/j.tsf.2008.07.014.
[50] F.M. Smits, Measurement of Sheet Resistivities with the Four-Point Probe, Bell System Technical Journal. 37 (1958) 711–718. https://doi.org/10.1002/j.1538-7305.1958.tb03883.x.
[51] N. Mattern, A. Schöps, U. Kühn, J. Acker, O. Khvostikova, J. Eckert, Structural behavior of CuxZr100−x metallic glass (x=35−70), Journal of Non-Crystalline Solids. 354 (2008) 1054–1060. https://doi.org/10.1016/j.jnoncrysol.2007.08.035.
[52] B.A. Movchan, A.V. Demchishin, Structure and properties of thick condensates of nickel, titanium, tungsten, aluminum oxides, and zirconium dioxide in vacuum, Fiz. Metal. Metalloved. 28 (1969) 653.

[53] J.A. Thornton, Influence of apparatus geometry and deposition conditions on the structure and topography of thick sputtered coatings, Journal of Vacuum Science and Technology. 11 (1974) 666–670. https://doi.org/10.1116/1.1312732.
[54] J.A. Thornton, High Rate Thick Film Growth, Annual Review of Materials Science. 7 (1977) 239–260. https://doi.org/10.1146/annurev.ms.07.080177.001323.
[55] P.B. Barna, M. Adamik, Fundamental structure forming phenomena of polycrystalline films and the structure zone models, Thin Solid Films. 317 (1998) 27–33. https://doi.org/10.1016/S0040-6090(97)00503-8.
[56] A. Anders, A structure zone diagram including plasma-based deposition and ion etching, Thin Solid Films. 518 (2010) 4087–4090. https://doi.org/10.1016/j.tsf.2009.10.145.
[57] P. Denis, H.-J. Fecht, Y. Xue, E.M. Paschalidou, P. Rizzi, L. Battezzati, Microstructure and electrochemical properties of nanoporous gold produced by dealloying Au-based thin film nanoglass, Journal of Materials Research. 33 (2018) 2661–2670. https://doi.org/10.1557/jmr.2018.176.
[58] P. Zeman, M. Zítek, Š. Zuzjaková, R. Čerstvý, Amorphous Zr-Cu thin-film alloys with metallic glass behavior, Journal of Alloys and Compounds. 696 (2017) 1298–1306. https://doi.org/10.1016/j.jallcom.2016.12.098.
[59] A. Rauf, C.Y. Guo, Y.N. Fang, Z. Yu, B.A. Sun, T. Feng, Binary Cu-Zr thin film metallic glasses with tunable nanoscale structures and properties, Journal of Non-Crystalline Solids. 498 (2018) 95–102. https://doi.org/10.1016/j.jnoncrysol.2018.06.015.
[60] G.I. Nkou Bouala, A. Etiemble, C. Der Loughian, C. Langlois, J.-F. Pierson, P. Steyer, Silver influence on the antibacterial activity of multi-functional Zr-Cu based thin film metallic glasses, Surface and Coatings Technology. 343 (2018) 108–114. https://doi.org/10.1016/j.surfcoat.2017.10.057.
[61] A. Brognara, J.P. Best, P. Djemia, D. Faurie, G. Dehm, M. Ghidelli, Effect of composition and nanostructure on the mechanical properties and thermal stability of Zr100-xCux thin film metallic glasses, Materials & Design. 219 (2022) 110752. https://doi.org/10.1016/j.matdes.2022.110752.
[62] M. Apreutesei, P. Steyer, A. Billard, L. Joly-Pottuz, C. Esnouf, Zr–Cu thin film metallic glasses: An assessment of the thermal stability and phases' transformation mechanisms, Journal of Alloys and Compounds. 619 (2015) 284–292. https://doi.org/10.1016/j.jallcom.2014.08.253.
[63] M. Apreutesei, A. Billard, P. Steyer, Crystallization and hardening of Zr-40at.% Cu thin film metallic glass: Effects of isothermal annealing, Materials & Design. 86 (2015) 555–563. https://doi.org/10.1016/j.matdes.2015.07.149.
[64] M. Apreutesei, C. Esnouf, A. Billard, P. Steyer, Impact of local nanocrystallization on mechanical properties in the Zr-59 at.% Cu metallic glass thin film, Materials & Design. 108 (2016) 8–12. https://doi.org/10.1016/j.matdes.2016.06.081.
[65] S. Comby-Dassonneville, G. Tiphéne, A. Borroto, G. Guillonneau, L. Roiban, G. Kermouche, J.-F. Pierson, J.-L. Loubet, P. Steyer, Real-time high-temperature scanning indentation: Probing physical changes in thin-film metallic glasses, Applied Materials Today. 24 (2021) 101126. https://doi.org/10.1016/j.apmt.2021.101126.
[66] D.B. Miracle, D.V. Louzguine-Luzgin, L.V. Louzguina-Luzgina, A. Inoue, An assessment of binary metallic glasses: correlations between structure, glass forming ability and stability, International Materials Reviews. 55 (2010) 218–256. https://doi.org/10.1179/095066010X12646898728200.
[67] D. Arias, J.P. Abriata, Cu-Zr (Copper-Zirconium), Bulletin of Alloy Phase Diagrams. 11 (1990) 452–459. https://doi.org/10.1007/BF02898260.

[68] D. Depla, B.R. Braeckman, Quantitative correlation between intrinsic stress and microstructure of thin films, Thin Solid Films. 604 (2016) 90–93. https://doi.org/10.1016/j.tsf.2016.03.039.
[69] F. Puosi, N. Jakse, A. Pasturel, Dynamical, structural and chemical heterogeneities in a binary metallic glass-forming liquid, J. Phys.: Condens. Matter. 30 (2018) 145701. https://doi.org/10.1088/1361-648X/aab110.
[70] A. Annamareddy, P.M. Voyles, J. Perepezko, D. Morgan, Mechanisms of bulk and surface diffusion in metallic glasses determined from molecular dynamics simulations, Acta Materialia. 209 (2021) 116794. https://doi.org/10.1016/j.actamat.2021.116794.
[71] P. Coddet, F. Sanchette, J.C. Rousset, O. Rapaud, C. Coddet, On the elastic modulus and hardness of co-sputtered Zr–Cu–(N) thin metal glass films, Surface and Coatings Technology. 206 (2012) 3567–3571. https://doi.org/10.1016/j.surfcoat.2012.02.036.
[72] D. You, H. Zhang, S. Ganorkar, T. Kim, J. Schroers, J.J. Vlassak, D. Lee, Electrical resistivity as a descriptor for classificatin of amorphous versus crystalline phases of alloys, Acta Materialia. 231 (2022) 117861. https://doi.org/10.1016/j.actamat.2022.117861.
[73] J. Houska, P. Machanova, M. Zitek, P. Zeman, Molecular dynamics and experimental study of the growth, structure and properties of Zr–Cu films, Journal of Alloys and Compounds. 828 (2020) 154433. https://doi.org/10.1016/j.jallcom.2020.154433.
[74] T. Egami, Y. Waseda, Atomic size effect on the formability of metallic glasses, Journal of Non-Crystalline Solids. 64 (1984) 113–134. https://doi.org/10.1016/0022-3093(84)90210-2.
[75] Z.T. Wang, K.Y. Zeng, Y. Li, The correlation between glass formation and hardness of the amorphous phase, Scripta Materialia. 65 (2011) 747–750. https://doi.org/10.1016/j.scriptamat.2011.06.043.
[76] D. Ma, A.D. Stoica, X.-L. Wang, Power-law scaling and fractal nature of medium-range order in metallic glasses, Nature Materials. 8 (2009) 30–34. https://doi.org/10.1038/nmat2340.
[77] N. Mattern, Comment on "Thermal expansion measurements by X-ray scattering and breakdown of Ehrenfest's relation in alloy liquids" [Appl. Phys. Lett. **104** , 191907 (2014)], Appl. Phys. Lett. 105 (2014) 256101. https://doi.org/10.1063/1.4904942.
[78] B.R. Braeckman, D. Depla, On the amorphous nature of sputtered thin film alloys, Acta Materialia. 109 (2016) 323–329. https://doi.org/10.1016/j.actamat.2016.02.035.
[79] J. Ding, M. Asta, R.O. Ritchie, On the question of fractal packing structure in metallic glasses, Proceedings of the National Academy of Sciences. 114 (2017) 8458–8463. https://doi.org/10.1073/pnas.1705723114.
[80] L. Xie, P. Brault, A.-L. Thomann, L. Bedra, Molecular dynamic simulation of binary ZrxCu100−x metallic glass thin film growth, Applied Surface Science. 274 (2013) 164–170. https://doi.org/10.1016/j.apsusc.2013.03.004.
[81] K.-W. Park, J. Jang, M. Wakeda, Y. Shibutani, J.-C. Lee, Atomic packing density and its influence on the properties of Cu–Zr amorphous alloys, Scripta Materialia. 57 (2007) 805–808. https://doi.org/10.1016/j.scriptamat.2007.07.019.
[82] Z. Altounian, T. Guo- hua, J.O. Strom- Olsen, Crystallization characteristics of Cu- Zr metallic glasses from Cu70Zr30 to Cu25Zr75, Journal of Applied Physics. 53 (1982) 4755–4760. https://doi.org/10.1063/1.331304.
[83] T.T. Hu, J.H. Hsu, J.C. Huang, S.Y. Kuan, C.J. Lee, T.G. Nieh, Correlation between reflectivity and resistivity in multi-component metallic systems, Applied Physics Letters. 101 (2012) 011902. https://doi.org/10.1063/1.4732143.

[84] S. Canulescu, C.N. Borca, K. Rechendorff, S. Daviðsdóttir, K. Pagh Almtoft, L.P. Nielsen, J. Schou, Optical and electrical properties of polycrystalline and amorphous Al-Ti thin films, Appl. Phys. Lett. 108 (2016) 141909. https://doi.org/10.1063/1.4945769.
[85] S. Babar, J.H. Weaver, Optical constants of Cu, Ag, and Au revisited, Appl. Opt., AO. 54 (2015) 477–481. https://doi.org/10.1364/AO.54.000477.
[86] W.H. Wang, J.H. Hsu, J.C. Huang, Optical reflectivity improvement by upgrading metallic glass film quality, Applied Physics Letters. 103 (2013) 161906. https://doi.org/10.1063/1.4825361.
[87] C.M. Chang, C.H. Wang, J.H. Hsu, J.C. Huang, Al–Ni–Y–X (X = Cu, Ta, Zr) metallic glass composite thin films for broad-band uniform reflectivity, Thin Solid Films. 571 (2014) 194–197. https://doi.org/10.1016/j.tsf.2014.10.048.